Scanning Microscopy

Volume 1993
Number 7 *Physics of Generation and Detection of Signals Used for Microcharacterization*

Article 18

1993

Computation of Scanning Tunneling Microscope Images of Nanometer-Sized Objects Physisorbed on Metal Surfaces

J. P. Vigneron
Univ. Notre-Dame de la Paix, Belgium

I. Derycke
Univ. Notre-Dame de la Paix, Belgium

Th. Laloyaux
Univ. Notre-Dame de la Paix, Belgium

Ph. Lambin
Belgian National Fund for Scientific Research

A. A. Lucas
Univ. Notre-Dame de la Paix, Belgium

Scanning Microscopy Supplement 7, 1993 (Pages 261-268) 0892-953X/93$5.00+.25
Scanning Microscopy International, Chicago (AMF O'Hare), IL 60666 USA

COMPUTATION OF SCANNING TUNNELING MICROSCOPE IMAGES OF NANOMETER-SIZED OBJECTS PHYSISORBED ON METAL SURFACES

J.P. Vigneron*, I. Derycke, Th. Laloyaux, Ph. Lambin[1] and A.A. Lucas

Institute for Studies in Interface Sciences, Facultés Univ. Notre-Dame de la Paix, B-5000 Namur, Belgium
[1]Research Associate of the Belgian National Fund for Scientific Research

Abstract

This communication deals with the application of a transfer-matrix strategy for the quantitative evaluation of the tunnel current in a scanning tunneling microscope (STM). The image given by a simple atomic-size object deposited on a metal surface is specifically examined in both modes of STM operation namely the constant-height and the constant-current modes. The two-dimensional corrugation induced at low temperature by Xe atoms physisorbed on an otherwise clean, unreconstructed Ni (110) surface is studied in detail. It is shown that the simple consideration of the elastic scattering of electrons by the three-dimensional potential barrier between the tip and the metal substrates provides a quantitative description of the images produced by the instrument: (1) the Xe atom appears as a conic protrusion, approximately 7 Å wide, with a corrugation 1.3 Å high; (2) in Xe clusters, each adjoining atom is resolved, with a shape in full agreement with experiment. In order to obtain correct quantitative results, image-charge corrections to the potential cannot be neglected.

Key Words: Tunneling, theory, adsorbate, physisorption, image, xenon, nickel, scattering, conductance, Laue representation.

*Address for correspondence:
J.P. Vigneron,
Inst. for Studies in Interface Sciences,
Facultés Univ. Notre-Dame de la Paix,
Rue de Bruxelles 61,
B-5000 Namur, Belgium.

Phone No.: 32-81-724711
Fax No.: 32-81-724707

Introduction

The topography of metal surfaces has been studied at very different scales, using various techniques. The ancestor of the scanning tunneling microscrope (STM), a field-emission tip carried by a piezoelectric tripod — the "topografiner" of Young *et al.* (Young *et al.*, 1971, 1972; Young, 1966, 1971) — could display the geometric corrugation of a metal surface with a lateral resolution of a few thousand Å, and a normal uncertainty reaching ten Å or so. Taking advantage of a much better mechanical stability, the scanning tunneling microscope of Binnig and Röhrer improved these figures by several orders of magnitude. The breakthrough was to succeed in bringing the tip and the scanned sample in close contact. By switching from the field-emission to the tunneling regime, the object is placed in the electron near-field evanescent waves of the tip and overcomes the quantum-mechanical diffraction effects.

The extreme localization of the probe calls for more care in the interpretation of the images. These cannot always be understood as reflecting the metal surface topography but rather as a signature of the tip and sample electronic structures. In other words, the STM image reflects the amount of overlap of the tip and sample wave functions at the tunneling energy: using the approximation introduced by Bardeen (Bardeen, 1961) and further simplifications later described by Tersoff and Hamann (Tersoff and Hamann, 1983, 1985; Hansma and Tersoff, 1987), the tunneling current reduces to the product of the Fermi-level tip density of states and the sample local density of states at the tip center of curvature. In the approach suggested by Sacks and Noguera (1991), the current relates to the local density of states of the coupled tip-sample system.

Because the charge density in conductors is strongly delocalized, their STM images usually appear to be weakly corrugated in spite of the fact that atomic resolution is undoubtedly reached by the instrument. The lack of corrugation can be seen as a drawback when one thinks of using the STM to assess crystallographic parameters, but it is actually a strong asset for the observation of isolated adsorbed objects. In such an observation, the metal surface plays the role of a sample

holder, and it is extremely valuable if the adsorbate is easily distinguished from its "background". This does not mean, however, that the substrate plays no role in the imaging process when the adsorbate is clearly contrasted. The adsorbate states are significantly modified by the proximity of the substrate and by the influence of the terminating atoms in the tip apex, especially when atomic-scale information is sought. The surface- and tip-induced broadening of the adsorbate states is of crucial importance as a sufficient broadening of the levels is necessary to provide density of states at the system Fermi level. In this situation, where the adsorbate becomes electronically bound both to the metal surface and to the tip, we cannot make use of rigid wave functions for the tip or the sample: because the states in the tip cluster and in the adsorbate extend well beyond the potential wells which control their localization, the wave functions in the tip and in the sample are distorted well before a perforation — or even a strong modification — of the potential barrier occurs (a situation which defines the atomic contact).

A reliable description of the scattering process taking place in the barrier starts with a careful description of the different elements in the potential energy and is followed by a very accurate representation of the associated scattered carrier wave functions. Such an approach, which improves on many computations based on the Bardeen transfer hamiltonian combined with approximate models of the tip and sample wave functions (Lang, 1985, 1986; Selloni *et al.*, 1985; Chung *et al.*, 1987; Leavens and Aerts, 1988), has been introduced by Lucas *et al.* (1988a, 1988b). Similar ideas have since been applied to solve more refined STM models (Doyen, 1990) or to exhibit more detailed information about the electron flow (Laloyaux *et al.*, 1988; Lucas *et al.*, 1992). In this work, a similar path is followed within the framework of a transfer-matrix approach. This method is used to model the STM operation on clusters of Xe atoms physisorbed at low temperature on a clean Ni (110) surface. The results of these simulations are compared with available experimental data.

Methodology

A detailed algebraic development of the transfer-matrix approach used to solve the three-dimensional scattering problem can be found in a specific paper by Derycke *et al.* (1991). This section only introduces those elements of the theory needed to correctly appreciate the content of the present simulations.

The region where the scattering takes place is the uniform gap between the planar surfaces of two free-electron metals (Figure 1). The first metal (I) carries

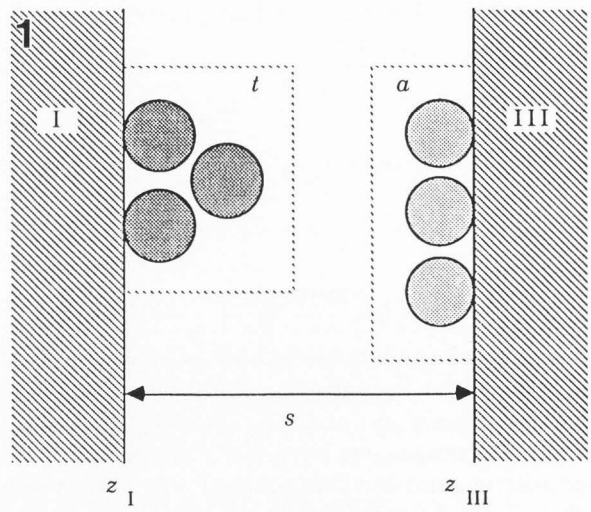

Figure 1. The tunneling takes place in the space separating a supported atomic-size cluster and a metallic sample holder carrying the adsorbate. The tunnel current depends on the three-dimensional electron scattering induced by the potential barrier corrugation.

---

the tip cluster (*t* on Figure 1) and the second metal (III) carries the adsorbate (*a* on Figure 1). The free-electron metals are each described by two parameters, the experimental work functions ϕ_S (sample side) and ϕ_T (tip side) (in the range 4-6 eV) and the bulk Fermi levels E_{FS} and E_{FT} (in the range 10-20 eV). At equilibrium (vanishing external bias *V*), the Fermi levels coincide so that the barrier between the planar metals has a trapezoidal shape with the top slightly tilted by the contact electric field arising from the difference in work functions. This trapezoidal barrier is further modified by the multiple image potential arising from the dynamic charge induced on both metal surfaces (Lucas *et al.*, 1984). The image potential has been shown to contribute a significant reduction of the barrier height in typical STM geometries (Persson and Baratoff, 1988). Imbedded in this one-dimensional potential, we then find the three-dimensional potential change induced by the presence of the cluster of atoms representing the tip apex and, on the other side, the cluster of atoms representing the adsorbate. These potential wells induced by the presence of these sharp protrusions inside the vacuum barrier will be replaced, in the present computations, by one-electron pseudopotentials, usually local and fitted to gaussian functions, for analytical convenience. The semi-infinite, flat metal support of the tip apex cluster is not quite a convincing representation of the macroscopic tip: the capacitor shape of the two metal holders at large distance from the tunneling channel generates a constant

current density which, for infinite plates, becomes infinite. Chosing finite-size planar holders is not a good idea as the computed current then experiences size effects and will be sensitive to the boundary conditions applied at the plate edges. Following a suggestion of Doyen, it is more appropriate to suppress this unphysical infinite capacitor leak current by analytically subtracting the planar capacitor contribution from the current produced by the corrugated plates. Several test cases have shown that on an absolute scale the current provided by this procedure is effectively independent of the lateral boundary conditions.

Images are generated by moving the tip cluster over the adsorbate at various, but fixed, tip-sample separations and by calculating the total current in the manner described below. From the stack of two-dimensional arrays of current values, simulated STM images are generated either by chosing a specific constant separation between the tip and the sample or by keeping the tunneling current constant.

The transfer-matrix approach of the tunneling current computation is basically borrowed from dynamic low-energy electron diffraction theory (Pendry, 1974). When a bias is applied to the junction between the metallic substrates, the resulting tunnel current arises from the unbalanced contributions of the incident waves transmitted from occupied states found in the tip and in the sample. If we assume, without loss of generality, that the sample is brought to a positive potential V, the current-carrying electrons have energies ranging from E_{FT} - eV - V_T and E_{FT} - V_T, where E_{FT} is the Fermi energy at the tip side and V_T is the average potential energy in the tip. These electrons are characterized by wavevectors $\boldsymbol{k}$ limited to the domain (we will refer to it as the "source domain κ") bound by the hemispheres of equations $\hbar^2k^2/2m = E_{FT}$ - eV - V_T and $\hbar^2k^2/2m = E_{FT}$ - V_T and further constraint by the requirement $k_z > 0$ (the z-axis is normal to the metal substrate surface and directed towards the sample). The enumeration of incident waves is made discrete by periodically repeating the tip and the adsorbate in both lateral x and y directions (coordinate ρ) in a supercell large enough to contain these clusters entirely and make negligible cell-to-cell interactions. The incident waves are then described as two-dimensional Bloch waves, which can be expanded into a two-dimensional Fourier series, leading to the so-called Laue (or $\boldsymbol{g}$-z) representation. In this representation, the wavevector $\boldsymbol{k}$ is naturally split into a Brillouin-zone vector $\boldsymbol{q}$ and a supercell reciprocal lattice vector $\boldsymbol{g}$:

$$\Psi_{(\boldsymbol{q},\boldsymbol{g})}(\boldsymbol{r}) = \sum_{\boldsymbol{g}'} \phi^{(\boldsymbol{q})}_{\boldsymbol{g}\boldsymbol{g}'}(z)\ e^{i\,(\boldsymbol{q}+\boldsymbol{g}')\cdot\boldsymbol{\rho}}. \tag{1}$$

The Schrödinger equation is then a linear system of complex ordinary differential equations

$$-\frac{\hbar^2}{2m}\frac{d^2\phi^{(\boldsymbol{q})}_{\boldsymbol{g}\boldsymbol{g}'}(z)}{dz^2} + \left(\frac{\hbar^2|\boldsymbol{q}+\boldsymbol{g}'|^2}{2m} - E\right)\phi^{(\boldsymbol{q})}_{\boldsymbol{g}\boldsymbol{g}'}(z) + \sum_{\boldsymbol{g}''} v_{\boldsymbol{g}'-\boldsymbol{g}''}(z)\ \phi^{(\boldsymbol{q})}_{\boldsymbol{g}\boldsymbol{g}''}(z) = 0 \tag{2}$$

which, if solved with the appropriate boundary conditions, provides the dynamic (i.e., multiply-scattered) wave functions needed to compute the current.

Three-dimensional tunneling boundary conditions

In the tip and the sample substrates, the potential keeps a constant value (V_T on the tip side and V_S on the sample side), and the general solution of the above system of one-dimensional Schrödinger equations can be written analytically. In the tip holder region (region I, $z < z_I$), we have

$$\sqrt{\Omega}\ \phi^{(\boldsymbol{q})}_{\boldsymbol{g}\boldsymbol{g}'}(z) = a^{+}_{\boldsymbol{g}'\boldsymbol{g}\mathrm{I}}\ e^{i\,k_{\boldsymbol{g}'\mathrm{I}}\,(z-z_I)} + a^{-}_{\boldsymbol{g}'\boldsymbol{g}\mathrm{I}}\ e^{-i\,k_{\boldsymbol{g}'\mathrm{I}}\,(z-z_I)} \tag{3}$$

where Ω is the plane wave normalization volume, and where the z-component (of positive real part) of the wavevector is given by

$$k_{\boldsymbol{g}'\mathrm{I}} = \sqrt{\frac{2m(E-V_T)}{\hbar^2} - |\boldsymbol{q}+\boldsymbol{g}'|^2} \tag{4}$$

while in the sample substrate region (region III, $z > z_{III}$), we have

$$\sqrt{\Omega}\ \phi^{(\boldsymbol{q})}_{\boldsymbol{g}\boldsymbol{g}'}(z) = a^{+}_{\boldsymbol{g}'\boldsymbol{g}\mathrm{III}}\ e^{ik_{\boldsymbol{g}'\mathrm{III}}(z-z_{III})} + a^{-}_{\boldsymbol{g}'\boldsymbol{g}\mathrm{III}}\ e^{-ik_{\boldsymbol{g}'\mathrm{III}}(z-z_{III})} \tag{5}$$

with a z-component of the wavevector given by

$$k_{\boldsymbol{g}'\mathrm{III}} = \sqrt{\frac{2m(E-V_S)}{\hbar^2} - |\boldsymbol{q}+\boldsymbol{g}'|^2} \tag{6}$$

The aim is now to study the scattering of a single incident wave of wavevector $\boldsymbol{q} + \boldsymbol{g}$, that is to find the continuous wave (with continuous first derivative) constrained by the conditions $a^{+}_{\boldsymbol{g}'\boldsymbol{g}\,\mathrm{I}} = \delta_{\boldsymbol{g}'\boldsymbol{g}}$ and $a^{-}_{\boldsymbol{g}'\boldsymbol{g}\,\mathrm{III}} = 0$. The transfer-matrix representation requires the following notation: we denote the matrix of coefficients $a^{+}_{\boldsymbol{g}'\boldsymbol{g}\,\mathrm{I}}$ by A^{+}_{I} and, similarly, $a^{-}_{\boldsymbol{g}'\boldsymbol{g}\,\mathrm{I}}$ by A^{-}_{I}, $a^{+}_{\boldsymbol{g}'\boldsymbol{g}\,\mathrm{III}}$ by A^{+}_{III}, and $a^{-}_{\boldsymbol{g}'\boldsymbol{g}\,\mathrm{III}}$ by A^{-}_{III}. It can be shown immediately that these

matrices are related by the following equation

$$\begin{bmatrix} A^{+}_{\mathrm{III}} \\ A^{-}_{\mathrm{III}} \end{bmatrix} = \begin{bmatrix} M^{++} & M^{+-} \\ M^{-+} & M^{--} \end{bmatrix} \begin{bmatrix} A^{+}_{\mathrm{I}} \\ A^{-}_{\mathrm{I}} \end{bmatrix} \tag{7}$$

and that the transfer matrix can be easily found from the following expressions

$$M^{++} = \left[\frac{1}{2}(\theta_{gg'} - \mathrm{i}\frac{\Delta_{gg'}}{k_{g\mathrm{III}}})\right], \quad M^{+-} = \left[\frac{1}{2}(\theta^{*}_{gg'} - \mathrm{i}\frac{\Delta^{*}_{gg'}}{k_{g\mathrm{III}}})\right]$$
$$M^{-+} = \left[\frac{1}{2}(\theta_{gg'} + \mathrm{i}\frac{\Delta_{gg'}}{k_{g\mathrm{III}}})\right], \quad M^{--} = \left[\frac{1}{2}(\theta^{*}_{gg'} + \mathrm{i}\frac{\Delta^{*}_{gg'}}{k_{g\mathrm{III}}})\right] \tag{8}$$

where

$$\theta_{g'g} = \sqrt{\Omega}\,\phi^{(q)}_{g'g}(z_{III}), \text{ and } \Delta_{g'g} = \sqrt{\Omega}\,\phi^{'(q)}_{g'g}(z_{III})$$

if

$$\sqrt{\Omega}\,\phi^{(q)}_{g'g}(z_I) = \delta_{g'g}, \text{and } \sqrt{\Omega}\,\phi^{'(q)}_{g'g}(z_I) = \mathrm{i}\ k_{g'\mathrm{I}}\ \delta_{g'g}$$

and where

$$\theta^{*}_{g'g} = \sqrt{\Omega}\,\phi^{(q)}_{g'g}(z_{III}) \text{ and } \Delta^{*}_{g'g} = \sqrt{\Omega}\,\phi^{'(q)}_{g'g}(z_{III})$$

if

$$\sqrt{\Omega}\,\phi^{(q)}_{g'g}(z_I) = \delta_{g'g}, \text{ and } \sqrt{\Omega}\,\phi^{'(q)}_{g'g}(z_I) = -\mathrm{i}\ k_{g'\mathrm{I}}\ \delta_{g'g}$$

These definitions must be understood as the result of the integration to z_{III} of the one-dimensional system (2) subject to the specified **initial conditions** imposed at z_{I}. The integration of the system can be carried out very efficiently using, for instance, an Adams multistep implicit scheme and accounting for the fact that the first derivatives do not appear in the Schrödinger equation. For local barrier potentials, the evaluation of the convolution product appearing in the differential equations can be done via the two-dimensional fast Fourier transform, and for non-local potentials, other fast procedures have been proposed (Gonze *et al.*, 1989). With these tools, the current computation can be carried out with high accuracy (typically, 256 ***g***-vectors can easily be kept for convergence) and still with enough efficiency to enable the generation of entire arrays of image pixels in a reasonable time.

The boundary conditions require the following values for the "known" matrices: $A^{+}_{\mathrm{I}} = 1$ and $A^{-}_{\mathrm{III}} = 0$ (in the matrix sense). From these conditions, the amplitudes of the wave reflected back into the tip can easily be computed as the solution of the algebraic system of linear equations:

$$M^{--}A^{-}_{\mathrm{I}} = -M^{-+}. \tag{9}$$

From this solution, the amplitude of the transmitted waves can also be computed:

$$A^{+}_{\mathrm{III}} = M^{++} + M^{+-}A^{-}_{\mathrm{I}}. \tag{10}$$

Tunneling current from the scattered wave function.

The total current which exits from a supercell can be computed by integrating the quantum mechanical expression of the current density over the area σ of this cell:

$$I = \int_{\sigma} J_z \ \mathrm{d}\rho^2. \tag{11}$$

If the integration surface is chosen to be a plane area parallel to the surface of the substrate, only the z-component of the current will be needed, as the surface element is directed along the z-axis: $dS = e_z d\rho^2$. Then, we are led to calculate this component of the current density by summing the contributions of all incident waves originating from the source domain κ, described above:

$$J_z(\boldsymbol{r}) = \frac{2\Omega}{8\pi^3} \int_{k_{\mathrm{F}}^{(1)}}^{k_{\mathrm{F}}^{(2)}} \mathrm{d}k \int_{S(k)} \mathrm{d}S \ j_z^{(\boldsymbol{q},\boldsymbol{g})}(\boldsymbol{r}). \tag{12}$$

Here, $j_z^{(\boldsymbol{q},\boldsymbol{g})}(\boldsymbol{r})$, the current density transported by the scattered wave function $\Psi_{(\boldsymbol{q},\boldsymbol{g})}(\boldsymbol{r})$, is given by

$$j_z^{(\boldsymbol{q},\boldsymbol{g})}(\boldsymbol{r}) = \mathrm{Re}\left[-\mathrm{i}\frac{\hbar}{m}\Psi^{*}_{(\boldsymbol{q},\boldsymbol{g})}(\boldsymbol{r})\frac{\partial\Psi_{(\boldsymbol{q},\boldsymbol{g})}(\boldsymbol{r})}{\partial z}\right], \tag{13}$$

$S(k)$ denotes the hemisphere of radius k, and $k^{F(1)}$ and $k_F^{(2)}$ are the inner and outer Fermi wavevectors limiting the domain κ. The surface integration can be carried out on the $k_z = 0$ circular projection of the hemisphere, and turn the integration over the sphere radii k into an energy integral. This leaves us with the following expression

$$J_z(\boldsymbol{r}) =$$
$$\frac{2m}{\hbar^2}\frac{\Omega}{8\pi^3} \int_{E_{\mathrm{F}}-eV}^{E_{\mathrm{F}}} \mathrm{d}E \sum_{\boldsymbol{g}} \int_{\mathrm{ZB}} \mathrm{d}\boldsymbol{q}^2 j_z^{(\boldsymbol{q},\boldsymbol{g})}(\boldsymbol{r})\frac{\Theta(k^2_{\boldsymbol{g}\mathrm{I}}(E))}{k_{\boldsymbol{g}\mathrm{I}}(E)} \tag{14}$$

where

$$k_{g\mathrm{I}}(E) = \sqrt{\frac{2m(E-V_{\mathrm{T}})}{\hbar^2} - |q+g|^2} \qquad (15)$$

in which the Bloch form of the scattered wave function can be inserted, to yield:

$$I = \mathrm{Re}\frac{2}{h}\int_{E_{\mathrm{F}}-eV}^{E_{\mathrm{F}}} \mathrm{d}E \frac{\sigma}{4\pi^2} \int_{\mathrm{ZB}} \mathrm{d}q^2 \left[\sum_{gg'} (-\mathrm{i})\ \sqrt{\Omega}\phi^{(q)*}_{gg'}(z)\frac{\mathrm{d}\sqrt{\Omega}\phi^{(q)}_{gg'}(z)}{\mathrm{d}z}\right]\frac{\Theta(k^2_{g\mathrm{I}}(E))}{k_{g\mathrm{I}}(E)}. \qquad (16)$$

For a weak applied external potential V, the current can be linearized, and it is advisable to compute the tunnel conductance which, for a vanishing bias, requires only the knowledge of the wave function at $E = E_{\mathrm{FT}}$:

$$e\frac{\partial I}{\partial V} = \mathrm{Re}\frac{2e^2}{h}\frac{\sigma}{4\pi^2} \int_{\mathrm{ZB}} \mathrm{d}q^2 \left[\sum_{gg'} (-\mathrm{i})\ \sqrt{\Omega}\phi^{(q)*}_{gg'}(z)\frac{\mathrm{d}\sqrt{\Omega}\phi^{(q)}_{gg'}(z)}{\mathrm{d}z}\right]\frac{\Theta(k^2_{g\mathrm{I}}(E))}{k_{g\mathrm{I}}(E)} \qquad (17)$$

In this expression, one recognizes the quantum Hall conductance $e^2/h = 1/25813\ \Omega^{-1}$.

We are now ready to relate this expression to the reflection coefficients calculated in the preceding section. The calculation leads to

$$e\frac{\partial I}{\partial V} = 2\frac{e^2}{h}\frac{\sigma}{4\pi^2}\int_{\mathrm{ZB}} \mathrm{d}q^2 \sum_{g} \Theta(k^2_{g\mathrm{I}}(E_{\mathrm{FT}})) \times \left[1 - \sum_{g'}\frac{k_{g'\mathrm{I}}(E_{\mathrm{FT}})}{k_{g\mathrm{I}}(E_{\mathrm{FT}})}\left|a^{-}_{g'g\mathrm{I}}\right|^2 \Theta(k^2_{g'\mathrm{I}}(E_{\mathrm{FT}}))\right] \qquad (18)$$

which can most easily be deduced, assuming the integration plane is pushed away to the remote region $z \approx -\infty$. By construction, however, the current remains constant for all position of this plane. As mentioned above, the expression of the conductance is sensitive to the size of our supercell and is not the appropriate expression to be compared to experiment. Our last step is then to subtract the reference (planar capacitor) current, an operation which removes the large (but unphysical) contribution brought in by the extended flat area surrounding the tip cluster and the adsorbate. Since the potential is not corrugated in the direction parallel to the substrate surface, the parallel momentum is conserved, and the coefficient matrices are immediately diagonal. The only coefficients needed are then explicitly given by

$$a^{-}_{gg\mathrm{I}} = \frac{\Delta_{gg} - \mathrm{i}\,k_{g\mathrm{III}}\ \Theta_{gg}}{\mathrm{i}\,k_{g\mathrm{III}}\ \Theta^{*}_{gg} - \Delta^{*}_{gg}} \qquad (19)$$

with the same meaning as before for the different terms Θ and Δ. These coefficients allow us to write the following final expression of the tunnel conductance:

$$e\frac{\partial(I-I_0)}{\partial V} = -2\frac{e^2}{h}\frac{\sigma}{4\pi^2}\int_{\mathrm{ZB}} \mathrm{d}q^2 \sum_{gg'} \frac{k_{g'\mathrm{I}}(E_{\mathrm{FT}})}{k_{g\mathrm{I}}(E_{\mathrm{FT}})} \times \Theta(k^2{}_{g\mathrm{I}}(E_{\mathrm{FT}}))\ \Theta(k^2{}_{g'\mathrm{I}}(E_{\mathrm{FT}})) \times \left[\left|a^{-}{}_{g'g\mathrm{I}}\right|^2 - \left|a^{-0}{}_{gg\mathrm{I}}\right|^2\delta_{g'g}\right] \qquad (20)$$

The following computation is the result of the application of this formula, including the reference current subtraction, to the simple case of a cluster of rare-gas atom physisorbed on a metal surface. The tip apex is reduced to a single atom but is carried by the surface of a flat, semi-infinite, free-electron metal holder.

Xe on Ni (110) Surface

Xe atoms have been observed as a very stable adsorbed system on the (110) nickel surface at cryogenic temperatures (Eigler *et al.*, 1991). Clusters of these atoms can be assembled by use of the tunnel tip and are stable enough to be scanned again afterwards. The image of a Xe atom produced by the STM under usual conditions is actually very simple: even in the case of several atoms in contact with each other, the constant-current surface has the shape of a rounded cone, with a basis diameter of 7 Å, and a height of about 1.6 Å. This roughly corresponds to the charge density contour, or the "shape", of the ion core of the Xe atom so that the image can be — naively — interpreted as a topographic image (Lang and Williams, 1982). It should be emphasized, however, that a STM image must be explained in terms of the tip, adsorbate, and substrate electronic structure interactions and, in particular, be put in relation with the changes of the scattered electron distribution as the tip position is varied. Standard semi-empirical quantum chemistry is now able to provide input to highly sophisticated and convincing STM simulations (Sautet and Joachim, 1992), including the case of adsorbate imaging (Cerda *et al.*, 1992). This is also what is done in the following simulation where specific

models have been designed to describe the scattering of electrons on the single atom apex of a tungsten tip, scanning a single Xe atom, or a group of three aligned Xe atoms, adsorbed on a Ni (110) surface.

The macroscopic single-atom-tip holder, considered to be tungsten, is modelled by a Sommerfeld metal surface, terminating abruptly at $z = z_I = 0$. The Fermi level E_{FT} is set to 19.1 eV above the constant effective potential V_T, and the work function ϕ_T is set to 4.6 eV. The tungsten apex atom is modelled as a gaussian pseudopotential well of depth chosen to be 24 eV and a radius of 1.6 Å with an adsorption distance of 2.7 Å relative to the Sommerfeld potential step. These values have been chosen to keep the model consistent with the Sommerfeld description of the tip holder: the tungsten atom well is then simply a gaussian attractive protrusion, sticking out of the planar tungsten surface. We use another Sommerfeld metal to model the sample holder beginning at $z = z_{III} = s$. The corresponding parameters for the nickel are the Fermi level E_{FS} and the work function ϕ_S set to 9.3 eV and 6.0 eV respectively. The Xe atom is also modelled by a gaussian pseudopotential well, with a standard spread parameter matching the Xe atomic radius of 1.14 Å and an adsorption distance of 1.7 Å measured from the center of the Xe atom to the edge of its supporting Ni Sommerfeld metal. This distance is equivalent to a Xe-Ni center-to-center separation of 2.4 Å or 4.5 bohr, comparable to the 5 bohr chosen by Eigler *et al.* The depth (178 eV) is chosen to bring the xenon p-state 7.6 eV below the Fermi level. This is the value suggested by the atomic calculation of Clementi *et al.* (Clementi and Roetti, 1974). The contact with the substrate may influence these values: photoemission measurements locate the $5p^{1/2}$ and $5p^{3/2}$ at 7.6 eV and 6 eV below the Fermi level, respectively. Changes of the adsorbate electronic structure are partially included (i.e., lacking self-consistency) in our calculation: the contact to the substrate turns the adsorbate bound states into scattering resonances, or "radiative states". Figure 2 shows a perspective view of the tunnel conductance as a function of the tip position, when the distance, relative to the potential steps, between the tip and the sample substrates is kept constant ($s = z_{III} - z_I = 8$ Å). The tunnel current is maximum, as expected, when the distance between the center of curvature of the tip and the center of the Xe atom is minimum. In this position [the W and the Xe atoms are then exactly in front of each other and separated by 5.5 Å or 10.5 bohr, a value quite close of the distance of 11 bohr chosen by Eigler *et al.* (1991)], the broadening of the p-states below the Fermi level and the unoccupied s-states, above, experiences a maximum. This broadening reinforces the density of states at the Fermi level which leads to an increase of the junction conductance. This effect is of course also expected when we consider an alignment of Xe atoms, but the quantitative question, here, is whether the theory predicts an atom image shape which allows to resolve each atom from its neighbors and whether the corrugation found in this simulation explains the value observed. Figure 3 shows the result for a group of three Xe atoms, as those prepared and observed by Eigler *et al.* (1991). The Xe atoms are located "on top" of selected atoms of the Ni (1x1) surface cell and are then separated by 4.9 Å. In the image computed with a fixed tip-to-substrate distance ($s = 8$ Å), the Xe atoms show up as protrusions which spread over a surface of about 30 $Å^2$. These images cannot however be compared directly to those shown in (Eigler *et al.*, 1991) as the latter are obtained in the constant-current mode of the STM. In order to simulate this mode by our computation, the current has been computed on various planes at different distances s and its logarithm interpolated as a function of s (using spline functions) at each lateral grid point. The constant-current surface ($I = 5$ nA for $V = 100$ mV) has then been extracted by a numerical zero-finder: the result is shown on Figure 4. It is interesting to note that in these images the Xe atoms are still represented by cones reaching a diameter of 7 Å, as experimentally observed. The contrast exhibited for the group of three Xe atoms compares very convincingly with the experimental constant-current surface: in particular, the fact that the saddle point between two atoms falls very precisely at the correct altitude (compared to the maximum found at the adatom center) essentially means that the simulation reproduces the correct cone width in units of the Xe-Xe distance. The corrugation is found to be 1.3 Å in this calculation, in good agreement with the experimental value of 1.6 Å.

These results show that the three-dimensional elastic electron scattering gives a convincing representation of the STM images of physisorbed Xe atoms. Some important limitations of this approach must be realized,

---

Figure 2. The Xe atom viewed by a simulated constant-height STM scan. The distance s between the sample holder and the tip substrate is chosen to be 8 Å. The quantity actually computed is the zero-bias conductance.

Figure 3. A group of three adjoining Xe atoms (4.9 Å from center to center) as viewed by a simulated constant-height STM scan. The zero-bias conductance is computed at a distance s between the sample holder and the tip substrate locked at 8 Å.

Figure 4. A group of three adjoining Xe atoms (4.9 Å from center to center) as viewed by a simulated constant-current STM scan. The constant conductance is chosen to be 50 $n\Omega^{-1}$ (tunnel resistance = 20 MΩ).

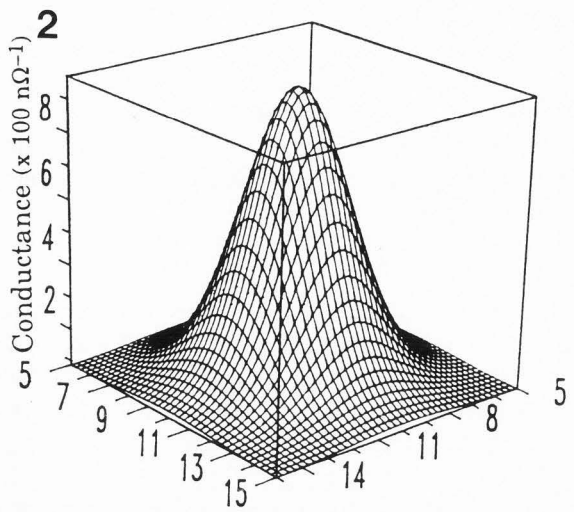

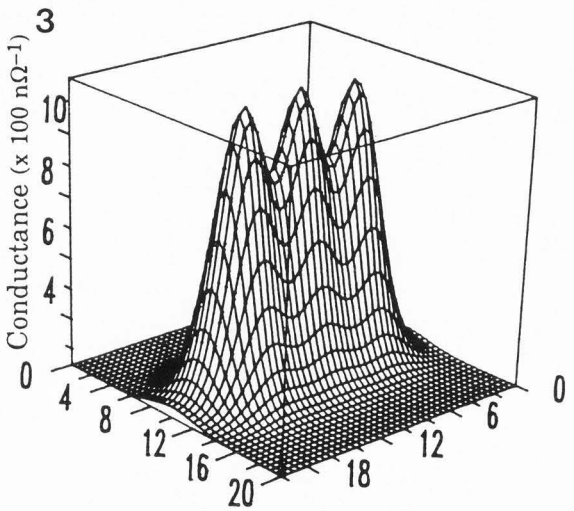

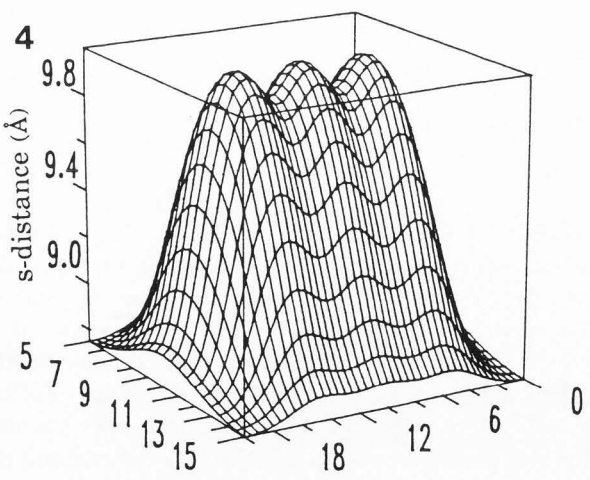

however, before building an objective appreciation of its generality: the main input to the simulation is the one-electron barrier potential, and this is not as easily described for all systems.

Acknowledgements

We are grateful to K. Kambe, M. Scheffler, G. Doyen and D. Drakova for discussions and many comments and suggestions during the development of this work. Part of this article presents research results of the Belgian Program of Interuniversity Attraction Poles initiated by the Belgian State-Prime Minister's Office-Science Policy Programming. The work was also partly funded by the Belgian national program of Interuniversity Research Projects initiated by the State-Prime Minister Office (Science Policy Programming): project ELSAM (Electronic Large Scale Computational System for Advanced Materials). We acknowledge the use of Namur Scientific Computing Facility (Namur-SCF), a common project of FNRS, IBM Belgium, and the Facultés Universitaires Notre-Dame de la Paix (FUNDP).

References

Bardeen J (1961) Tunneling from a many particle point of view. Phys. Rev. Lett. **6**, 57-69.

Cerda JR, de Andres PL, Flores F, Perez R (1992) Transport of physisorbed Xe atoms on Ni(110) using a scanning tunneling microscope: A theoretical approach. Phys. Rev. **B45**, 15, 8721-8729.

Chung MS, Feuchtwang TE, Cutler PH (1987) Spherical tip model in the theory of STM. Surf. Sci. **187**, 659-568.

Clementi E, Roetti C (1974) Roothaan-Hartree-Fock atomic wave functions. In: Atomic Data and Nuclear Data Tables. Way K (ed.). Academic Press, N.Y., Vol. **14**, Nb. 3-4.

Derycke I, Vigneron JP, Lambin Ph, Laloyaux Th, Lucas AA (1991) Computation of scanning tunneling microscope images. Int. J. Quant. Chem.: Quantum Chemistry Symposium **25**, 687-702.

Doyen G, Koetter E, Vigneron JP, Scheffler M (1990) Theory of scanning tunneling microscopy. Appl. Phys. **A51**, 281-288.

Eigler DM, Weiss PS, Schweitzer EK, Lang ND (1991) Imaging xenon with a low temperature scanning tunneling microscope. Phys. Rev. Lett. **66**, 1189-1192.

Gonze X, Vigneron JP, Michenaud JP (1989) Fast diagonalisation of non-local pseudopotential hamiltonians. J. Phys.: Condensed Matter **1**, 525-533.

Hansma P, Tersoff J (1987) Scanning tunneling microscopy. J. Appl. Phys. **61** (2), 1-23.

Laloyaux Th, Lucas AA, Vigneron JP, Lambin Ph, Morawitz H (1988) Lateral resolution of the scanning

tunneling microscope. J. Microsc. **152**, 53-63.

Lang ND (1985) Vacuum tunneling current from an adsorbed atom. Phys. Rev. Lett. **55**, 230-233. Errata: **55**, 2925.

Lang ND (1986) Theory of single-atom imaging in the scanning tunneling microscope. Phys. Rev. Lett. **56**, 1164-1167.

Lang ND, Williams AR (1982) Theory of local-work-function determination by photoemission from rare-gas adsorbates. Phys. Rev. **B25**, 2940-2946.

Leavens CR, Aerts GC (1988) Tunneling current density within Tersoff and Hamann's theory of the scanning tunneling microscope. Phys. Rev. **B38**, 7357-7364.

Lucas AA, Vigneron JP, Bono J, Cutler PH, Feuchtwang TE, Good Jr RH, Huang Z (1984) Potential distribution in metal-vacuum-metal planar barriers containing spherical protrusions or inclusions, J. Phys. Colloid Chem. **C9**, 125-132.

Lucas AA, Morawitz H, Henry GR, Vigneron JP, Lambin Ph, Cutler PH, Feuchtwang TE (1988a) Scattering-theoretic approach to elastic one-electron tunneling through localized barriers: Application to scanning tunneling microscopy. Phys. Rev. **B37**, 10708-10720.

Lucas AA, Morawitz H, Henry GR, Vigneron JP, Lambin Ph, Cutler PH, Feuchtwang TE (1988b) Tunneling through localized barriers with application to scanning tunneling microscopy: New scattering approach and results. J. Vac. Sci. Technol. **A6**, 296-299.

Lucas AA, Vigneron JP, Lambin Ph, Laloyaux Th, Derycke I (1992) Theoretical aspects of scanning tunneling microscopy. Surface Science **269/270** 74-80.

Pendry JB (1974) Low Energy Electron Diffraction. Academic Press, London.

Persson BNJ, Baratoff A (1988) Self-consistent dynamic image potential in tunneling. Phys. Rev. **B38**, 9616-9627.

Sacks W, Noguera C (1991) Generalized expression for the tunneling current in scanning tunneling microscopy. Phys. Rev. **B43**, 11612-11622.

Sautet Ph, Joachim C (1992) Interpretation of STM images: Copper-phthalocyanine on copper. Surf. Sci. **271**, 387-394.

Selloni A, Carnevali P, Tosatti E, Chen CD (1985) Voltage-dependent scanning-tunneling microscopy of a crystal surface: Graphite. Phys. Rev. **B31**, 2602-2605. Erratum: (1986) Phys. Rev. **B34**, 7406.

Tersoff J, Hamann DR (1983) Theory and application for the scanning tunneling microscope. Phys. Rev. Letters **50**, 1998-2001.

Tersoff J, Hamann DR (1985) Theory of the scanning tunneling microscope. Phys. Rev. **B31**, 805-813.

Young RD (1966) Field emission ultramicrometer. Rev. Sci. Instrum. **37**, 275-278.

Young RD (1971) Surface microtopography. Phys. Today **Nov. 1971**, 42-49.

Young RD, Ward J, Scire F (1971) Obervation of metal-vacuum-metal tunneling, field emission, and the transition region. Phys. Rev. Lett. **27**, 922-924.

Young RD, Ward J, Scire F (1972) The topographiner: An instrument for measuring surface microtopography. Rev. Sci. Instrum. **43**, 999-1011.

Discussion with Reviewers

R.S. Becker: How would the corrugation and appearance of the Xe atoms change if the probe atom was modeled using other than Gaussian (s-wave) wave functions? In other words, what would the relative effect of p_z- or d-states have on the computed image?

Authors: We have examined different potential models to represent the tip, including wells which support s-waves. The results are not qualitatively different for the following reason: an s-wave intrinsically gives a broader image than p- or d-states at the same tip-sample distance. However, to maintain a similar level of current, it is advisable in the case of a s-state to reduce the tip-sample distance, an operation which tends to partially restore the resolution.

R.S. Becker: Do you think that careful simulations along these lines may eventually allow the STM to be utilized in quantitative measurements of surface atom vertical and lateral positions to an accuracy greater than 0.1 Å?

Authors: The agreement with the experiment on this simple system (1.3 Å corrugation against 1.5 experimentally) is very promising. We tend to believe that the difference may be due to a substantial relaxation of the tip-Xe distance occuring during the scan. These deformations are not accounted for in the present simulation. Thus, we believe there is a good chance that this type of study can effectively help extract quantitative information from STM scans.

W. Sachs: As pointed out, one expects tip-surface interactions to be important in this case. Indeed, your calculation scheme includes (although not self-consistently) some of these effects. Unfortunately, you reach no conclusions on this from your results.

Authors: It is difficult to explain the large contrast observed when imaging Xe on Ni because none of the adsorbed Xe states lies close to the tunneling energy. Therefore, in the description of these images, it is crucial to include the contribution of the tip states to the Fermi level density of states. This is the virtue of the present approach to simultaneously incorporate the multiple scattering on the tip apex and the sample and describe the distortion of the wave functions because of the tip-sample interaction.